PAPER

Metal–organic framework-derived trimetallic oxides with dual sensing functions for ethanol†

Xin-Yu Huang, [ID] [a] Ya-Ru Kang, [b] Shu Yan, [ID] [a] Ahmed Elmarakbi, [ID] [c] Yong-Qing Fu [ID] *[c] and Wan-Feng Xie [ID] *[a,d]

Metal–organic framework (MOF)-derived metal oxide semiconductors have recently received extensive attention in gas sensing applications due to their high porosity and three-dimensional architecture. Still, challenges remain for MOF-derived materials, including low-cost and facile synthetic methods, rational nanostructure design, and superior gas-sensing performances. Herein, a series of Fe-MIL-88B-derived tri-metallic FeCoNi oxides (FCN-MOS) with a mesoporous structure were synthesized by a one-step hydro-thermal reaction followed by calcination. The FCN-MOS system consists of three main phases: α-Fe$_2$O$_3$ (n-type), CoFe$_2$O$_4$, and NiFe$_2$O$_4$ (p-type), and the nanostructure and pore size can be controlled by alter-ing the content of α-Fe$_2$O$_3$, CoFe$_2$O$_4$, and NiFe$_2$O$_4$. The sensors based on FCN-MOS exhibit a high response of 71.9, a good selectivity towards 100 ppm ethanol at 250 °C, and long-term stability up to 60 days. Additionally, the FCN-MOS-based sensors show a p–n transition gas sensing behavior with the alteration of the Fe/Co/Ni ratio.

Introduction

Metal–organic frameworks (MOFs), a network with a three-dimensional porous structure and a large specific surface area, are constructed *via* coordination bonds between inorganic nodes and organic ligands.[1–4] Compared to the most MOFs containing divalent metal cations, Fe-MOFs are more robust porous frameworks linked by trivalent metals.[5] Among the well-known Fe^{3+}-terephthalate MOFs, Fe-MIL-88B is a flexible framework with a three-dimensional hexagonal structure and exhibits continuous breathing during solvation/desolvation.[6,7] Considering the outstanding nature of MOFs, recently, tremen-dous attention has been paid to the development of MOF-derived metal oxide semiconductors (MOSs).[8,9] MOF-derived MOS materials exhibit multifunctional characteristics and have been utilized in various applications such as catalysis,[10] oxygen evolution reactions,[11,12] and ion batteries.[13]

In the past few decades, various gas sensors have been developed for monitoring different gases. Among them, chemi-

resistive sensors are widely used for gas detection, owing to their portable and low-cost properties.[14,15] Most chemiresistive sensors are MOS-based and operate at relatively high tempera-tures (typically around 300 °C) to achieve better sensing performances.[16,17] However, MOFs cannot remain stable at such high temperatures because of the poor thermal stability of their organic skeleton. Besides, it is hard to effectively obtain the sensing signal of MOFs due to their poor electrical conductivity, and a few studies directly applied MOFs on chemiresistive sensors. To overcome the above limitation, it is feasible and promising to utilize MOF-derived MOSs as sensing materials, which can effectively optimize the nano-structure and increase the active sites of sensing materials, thus improving the gas-sensing performance further.

To date, many polymetallic oxides have been developed for gas sensing using bimetallic or trimetallic MOFs as templates. Introducing different metal ions into MOF-derived MOS systems can effectively increase their active sites and conduc-tivity, leading to an improvement of the physicochemical reac-tion rates of target analytes.[18,19] Accordingly, Fe-MIL-88B-derived polymetallic oxides are promising candidates to enhance gas sensing. Typically, the direct sacrifice of Fe-MIL-88B can obtain the monometallic oxide of α-Fe$_2$O$_3$, an n-type semiconductor with a bandgap (E_g) of 2.2 eV, which is often utilized for chemiresistive gas sensors.[17] By doping the Fe-MIL-88B template with heteroatoms of similar periods, polymetallic oxides consisting of MFe$_2$O$_4$-based spinels can be formed. (M = Ni, Co, Zn, and Mn). Furthermore, MFe$_2$O$_4$-based spinels also show good gas-sensing performance.[17] Among

[a]*College of Electronics and Information, University-Industry Joint Center for Ocean Observation and Broadband Communication, Qingdao University, Qingdao 266071, P. R. China. E-mail: wfxie@qdu.edu.cn*
[b]*School of Integrated Circuits, University of Chinese Academy of Sciences, Beijing 100049, P. R. China*
[c]*Faculty of Engineering and Environment, Northumbria University, Newcastle upon Tyne NE1 8ST, UK. E-mail: richard.fu@northumbria.ac.uk*
[d]*Department of Physics, Dongguk University, Seoul 04620, South Korea*
†Electronic supplementary information (ESI) available. See DOI: https://doi.org/10.1039/d3nr00841j

them, $CoFe_2O_4$ and $NiFe_2O_4$ spinel oxides, which are widely applied in chemiresistive gas sensors, are p-type semiconductor materials with bandgaps of 0.8 and 1.3 eV, respectively.[20,21] For example, double-shelled nanocubes of $Co_3O_4/CoFe_2O_4$ show a response of 12.7 toward 10 ppm formaldehyde with a fast response/recovery speed (4/9 s) and an LOD of 300 ppb;[22] hierarchically double-shelled hollow spheres of $CoFe_2O_4$ exhibit high sensitivity to ammonia gas at 240 °C;[20] superfine and porous $NiFe_2O_4$ microspheres exhibit a high selectivity to acetone against other interfering gases, with a sensitivity of 27.4, an LOD of 200 ppb, and a fast response time of 2 s towards 100 ppm acetone;[23] α-$Fe_2O_3/NiFe_2O_4$ nanotubes with a large specific surface area (118.03 m^2 g^{-1}) exhibit excellent sensing performance, including good sensitivity (23), a fast response speed (4 s), and long-term stability (30 days) towards 100 ppm acetone at 200 °C.[24] Hence, it is worthwhile to develop α-Fe_2O_3, $CoFe_2O_4$, and $NiFe_2O_4$ nanocomposites as gas-sensing materials by using the Fe-MOF template doped with Co and Ni heteroatoms.

In this work, a series of Fe-MIL-88B-derived trimetallic FeCoNi metal oxide semiconductors (FCN-MOS) with a mesoporous nanostructure were successfully synthesized by a one-step hydrothermal reaction followed by calcination treatment. By optimizing the ratio of α-Fe_2O_3 and MFe_2O_4 in the FCN-MOS system, the nanostructure and pore size can be effectively tuned, resulting in the enhancement of gas-sensing performance. The FCN-MOS with the optimal molar ratio ($Fe:Co:Ni = 7:1.5:1.5$) has an elongated hexagonal rod-like structure with abundant mesopores and a large specific area. The sensor based on $Fe_7Co_{1.5}Ni_{1.5}$ shows high sensitivity ($S = 71.9$), long-term stability, and good selectivity for ethanol at the optimal working temperature of 250 °C. Besides, an interesting p–n gas-sensing transition behavior was observed when varying the Fe/Co/Ni ratio, and the sensing mechanism was fully discussed.

Experimental

Synthesis of FCN-MOSs

All the chemicals were purchased from Aladdin Industrial Corporation and used without purification. These include ferric trichloride ($FeCl_3 \cdot 6H_2O$), cobalt(II) acetate tetrahydrate ($Co(Ac)_2 \cdot 4H_2O$), nickel(II) acetate tetrahydrate ($Ni(Ac)_2 \cdot 4H_2O$), p-phthalic acid (1,4-BDC), N,N-dimethylformamide (DMF), acetone (C_3H_6O), and ammonia ($NH_3 \cdot H_2O$).

A series of MOF-derived MOSs were synthesized using a hydrothermal method with the following calcination treatment. Generally, 1 mmol of $FeCl_3 \cdot 6H_2O$ was dissolved in 20 mL of a mixed solvent of DMF and acetone (with a volume ratio of 1:1) to form solution A. 1 mmol of 1,4-BDC was dissolved in 10 ml of a mixed solvent of DMF and acetone (volume ratio is 1:1) to form solution B. Then, solution A was poured into solution B and magnetically stirred for 1 h at room temperature, while adding 100 μL of ammonia solution. The mixed solution was poured into a Teflon-lined stainless-steel autoclave (50 mL) and was heated to 120 °C for 24 h. The obtained products were washed with deionized water and absolute ethanol three times, followed by centrifugation, and then dried at 70 °C for 12 h in an oven. Finally, the samples were calcined in a muffle furnace at 500 °C for 3 h in an ambient environment. The calcined products were collected for analysis. Similarly, other types of FCN-MOSs were also prepared using the same procedures but with different Fe, Co, and Ni ratios. For convenience, these FCN-MOSs of $Fe_7Co_{1.5}Ni_{1.5}$, $Fe_6Co_2Ni_2$, $Fe_4Co_4Ni_2$ and $Fe_2Co_6Ni_2$ were named according to their molar ratios of 7:1.5:1.5, 6:2:2, 4:4:2 and 2:6:2 of $FeCl_3 \cdot 6H_2O$ /$Co(Ac)_2 \cdot 4H_2O/Ni(Ac)_2 \cdot 4H_2O$, respectively.

Sensor fabrication and measurement

For sensing layers, first, FCN-MOSs (including $Fe_7Co_{1.5}Ni_{1.5}$, $Fe_6Co_2Ni_2$, $Fe_4Co_4Ni_2$, and $Fe_2Co_6Ni_2$) were grounded thoroughly in ethanol in an agate mortar to obtain a homogeneous paste, which was uniformly coated onto the surface of an alumina ceramic tube and dried at 70 °C under vacuum for 12 h to form a gas-sensing layer. Gas-sensing tests were performed using a WS-30A gas-sensing measurement system (Zhengzhou Winsen Electronic Technology Co., Ltd, China). During the tests, the target gases with the given concentrations were injected into the evaporation platform of a test chamber (18 L) via a micro syringe. The substrate platform was heated to evaporate the liquid target analyte, and then the targeted gas was evenly distributed in the test chamber after diffusion using an air circulation device. When the resistance reading of the sensor became stable, the test chamber was lifted open to introduce the ambient air. The response (S) of the gas sensor can be calculated from $S = R_a/R_g$ (n-type) or $S = R_g/R_a$ (p-type), where R_a and R_g represent the resistance values of the sensor in air and in the testing gases, respectively.

Characterization

The surface morphology of the synthesized FCN-MOSs was characterized using a field emission scanning electron microscope (FE-SEM, Zeiss Gemini 500, Germany). Elemental mapping of the samples was performed using an energy-dispersive X-ray spectroscope (EDS, Oxford Link-ISIS 300, UK) operated at 15 kV. Crystal structures of the FCN-MOSs were studied using high-resolution transmission electron microscopy (HR-TEM, JEOL-2100 F, Japan), and interplanar spacings of lattice fringes were obtained using data analysis software (Gatan Digital Micrograph, USA). X-ray diffraction (XRD) was used to study the crystalline structure of the FCN-MOSs and was carried out using a Bruker D8 diffractometer equipped with Cu Kα radiation ($\lambda = 0.154$ nm). X-ray photoelectron spectroscopy (XPS) was used to determine the surface elemental composition and the chemical state of bonds of the FCN-MOSs, and an Escalab 250xi instrument (Thermo Scientific, USA) equipped with a monochromatic Al Kα source was used. The specific surface area and the pore size were determined by nitrogen (N_2) adsorption–desorption measurement using Brunner–Emmett–Teller (BET) and

Barrett–Joyner–Halenda (BJH) methods (Autosorb iQ Station 1, USA).

Results and discussion

Characterization of FCN-MOSs

In this work, MOF-derived MOS materials were synthesized *via* a one-step hydrothermal method and after calcination treatment using the Fe-MIL-88B template. A series of FeCoNi-trimetallic oxides were obtained, and the overall design and implementation processes are systematically illustrated in Scheme 1.

The morphologies of the Fe-MIL-88B template and its derivative were characterized by FE-SEM. The SEM images in Fig. S1† indicate that Fe-MIL-88B is a well-defined uniform hexagonal rod with pointed ends, which is consistent with previous reports.[25,26] The SEM images of $Fe_7Co_{1.5}Ni_{1.5}$ (Fig. 1a–c) show that the sample possesses an elongated hexagonal rod structure with an average length of 587 nm (Fig. S2†), similar to that of the MOF template. Furthermore, it can be observed that many nanoparticles are scattered on the sample surface and accumulate to form mesopores. For comparisons, the surface morphologies of $Fe_6Co_2Ni_2$, $Fe_4Co_4Ni_2$, and $Fe_2Co_6Ni_2$ were also characterized (Fig. S3†). The results reveal that the $Fe_6Co_2Ni_2$ and $Fe_4Co_4Ni_2$ samples maintain an elongated hexagonal structure, and the nanoparticle sizes become larger as the Fe/Ni ratios decrease. However, for $Fe_2Co_6Ni_2$, the structure became amorphous but still consisted of many nanoparticles.

TEM analysis was also performed to further investigate the morphology and structure. As shown in Fig. S4,† the Fe-MIL-88B template has a solid bulky rod-like structure with sharp edges. TEM images of $Fe_7Co_{1.5}Ni_{1.5}$ (Fig. 1d and e) further confirm that the sample is composed of nanoparticles ranging in size from 6 to 18 nm, with an average size of approximately 11 nm (Fig. S5†). The HR-TEM image (Fig. 1f) reveals distinctive spacings of 0.368 and 0.220 nm corresponding to the (012) and (006) lattice planes of α-Fe_2O_3, and
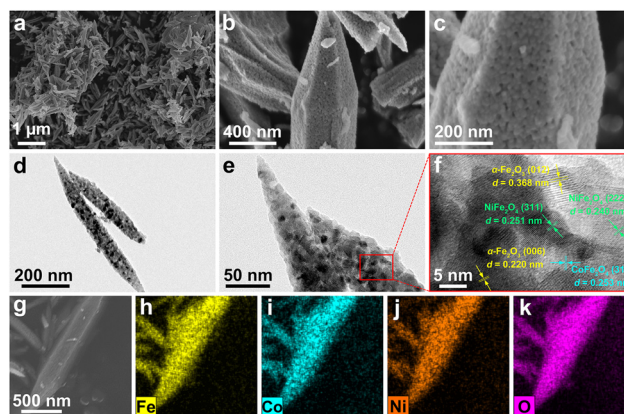

Fig. 1 (a–c) SEM images of $Fe_7Co_{1.5}Ni_{1.5}$ at different magnifications. (d–f) TEM and HR-TEM images of $Fe_7Co_{1.5}Ni_{1.5}$. (g) EDS mapping images of (h) Fe, (i) Co, (j) Ni, and (k) O elements distributed at $Fe_7Co_{1.5}Ni_{1.5}$.

the (222) and (311) lattice planes of $NiFe_2O_4$ are 0.251 and 0.240 nm, respectively, whereas that of the (311) lattice plane of $CoFe_2O_4$ is 0.253 nm. The elements of Fe, Co, Ni, and O (Fig. 1h–k) are consistently distributed across the selected scanning area (Fig. 1g) from the EDS elemental mapping results, demonstrating that the acquired sample is constituted of Fe, Co, Ni, and O elements. The EDS spectrum (Fig. S6†) shows that $Fe_7Co_{1.5}Ni_{1.5}$ contains 39.78% Fe, 1.52% Co and 15.47% Ni in atomic percentage, and the remaining concentration is oxygen.

It is vital to investigate the specific surface area and the pore size distribution of the MOF template and its derivative material. Hence, N_2 adsorption–desorption measurements were carried out. Both samples show the H4 isotherm curves (Fig. S7†).[27] The specific surface area of Fe-MIL-88B is calculated to be 55.70 m^2 g^{-1} (Fig. S7a†) and has a high meso-microporosity (Fig. S7b†). The sample $Fe_7Co_{1.5}Ni_{1.5}$ has a specific surface area of 39.51 m^2 g^{-1} (Fig. S7c†) and a uniform distribution of main mesopores of about 8 nm (Fig. S7d†). The BET and BJH results demonstrate that using MOFs as a template to drive metal oxides can effectively obtain a relatively high specific surface area and abundant mesoporous.

The XRD pattern of the prepared Fe-MIL-88B is shown in Fig. S8,† for which the characteristic peaks correlate well to previous reports, demonstrating the successful synthesis of Fe-MIL-88B.[7,25,26] Fig. 2a indicates that the crystalline phases of α-Fe_2O_3, $CoFe_2O_4$, and $NiFe_2O_4$ are detected in $Fe_7Co_{1.5}Ni_{1.5}$, $Fe_6Co_2Ni_2$, and $Fe_4Co_4Ni_2$, without the diffraction peaks of other phases. The observed diffraction peaks can be readily indexed to the crystal planes of α-Fe_2O_3 (PDF#33-0664), $CoFe_2O_4$ (PDF#03-0864), and $NiFe_2O_4$ (PDF#54-0964) phases, respectively, which agree well with the values from the powder diffraction file documents (Table S1†). The enlarged pattern in Fig. 2b shows that the intensity of the peak assigned to α-Fe_2O_3 (104) gradually decreases with the Fe/Ni ratio.

As it is well known, α-Fe_2O_3, an n-type sensing material, plays a critical role in enhancing the sensing performance.
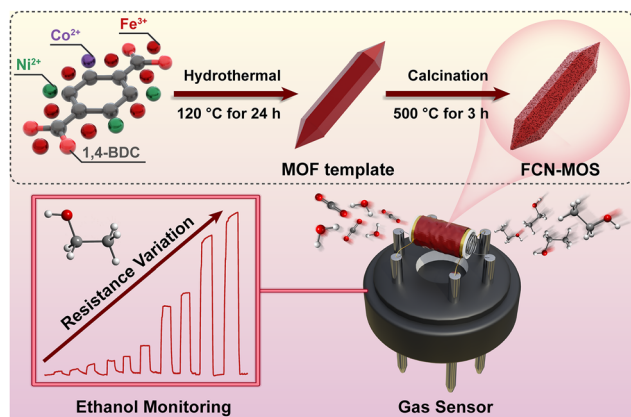
Scheme 1 The formation processes of FCN-MOS materials and the as-fabricated sensors.
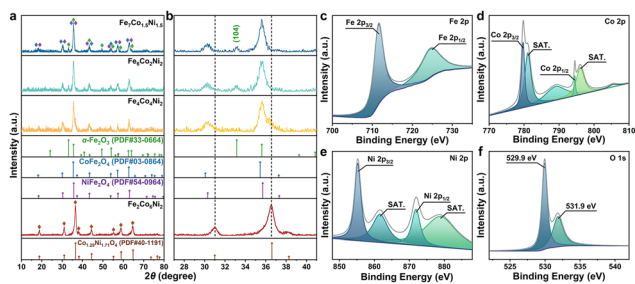
Fig. 2 (a and b) XRD patterns of $Fe_7Co_{1.5}Ni_{1.5}$, $Fe_6Co_2Ni_2$, $Fe_4Co_4Ni_2$, and $Fe_2Co_6Ni_2$. High-resolution XPS spectra of $Fe_7Co_{1.5}Ni_{1.5}$ for (c) Fe 2p, (d) Co 2p, (e) Ni 2p, and (f) O 1s.

Therefore, the XRD results imply that the high α-Fe_2O_3 ratio of the samples (*i.e.*, $Fe_7Co_{1.5}Ni_{1.5}$ and $Fe_6Co_2Ni_2$) might have excellent gas sensing properties. However, for the sample of $Fe_4Co_4Ni_2$, as the α-Fe_2O_3 content is reduced with the decrease of Fe element proportion, the sensor based on $Fe_4Co_4Ni_2$ might exhibit a transition from n-type to p-type sensing behavior accompanied by the deteriorated sensing performance. Nevertheless, it was found that the $Fe_2Co_6Ni_2$ sample is composed of $Co_{1.29}Ni_{1.71}O_4$ (PDF#40-1191) (Table S1†). The different crystalline structures of $Fe_2Co_6Ni_2$ are attributed to the relatively low Fe ratio in the FCN-MOS, which results in the absence of the α-Fe_2O_3 phase and the formation of a $Co_{1.29}Ni_{1.71}O_4$ phase. Therefore, the change in $Fe_2Co_6Ni_2$ composition leads to morphology and structure conversion, further affecting its gas-sensing properties. XRD pattern of pristine α-Fe_2O_3 is shown in Fig. S9,† corresponding to the phase of α-Fe_2O_3 (PDF#33-0664).

The XPS survey spectrum of $Fe_7Co_{1.5}Ni_{1.5}$ (Fig. 2c–f) shows the peaks of Fe 2p, Co 3d, Ni 3d, and O 1s. In the high-resolution spectrum of Fe 2p (Fig. 2c), two distinct peaks are observed at 711.6 eV for Fe $2p_{3/2}$ and 724.9 eV for Fe $2p_{1/2}$, corresponding to Fe^{3+} ions.[28] The energy gap of 13.3 eV between these two peaks is close to the values reported in the standard spectrum of Fe 2p. In the Co 2p spectrum (Fig. 2d), there are two peaks located at 779.7 and 794.5 eV, which are associated with the valence states of Co^{+2} for Co $2p_{3/2}$ and Co $2p_{1/2}$, respectively.[29] In the Ni 2p spectrum (Fig. 2e), two peaks at 855.2 and 871.9 eV correspond to Ni $2p_{3/2}$ and $2p_{1/2}$, respectively were observed. The Ni^{2+} and Ni^{3+} peaks have two satellite peaks of $2p_{3/2}$ and $2p_{1/2}$ at approximately 861.6 and 878.8 eV.[30] The O 1s spectrum (Fig. 2f) contains two peaks centered at 529.9 and 531.9 eV, representing lattice oxygen and chemisorbed oxygen, respectively.[31] The existence of chemisorbed oxygen is due to the surface chemisorbed O_2 molecules, which is favorable for detecting the response of the target gas molecules.

The sensitivity of the FCN-MOS-based sensors substantially depends on the operating temperature. It is reported that conduction band electrons (e^-) are dependent on the temperature, doping element, and volume mainly. The excited temperature (T) generates the electron concentration (n_0) in the conductive

band (E_c) for a semiconductor material, which is shown in eqn (1):[32]

$$n_0 = 2\left(\frac{m_n^* k_0 T}{2\pi\hbar^2}\right)^{\frac{3}{2}} \exp\left(-\frac{E_C - E_F}{k_0 T}\right) \quad (1)$$

where m_n^* is the effective mass of the electron, k_0 is Boltzmann's constant, h is Planck's constant, $\hbar = h/2\pi$, and E_F is the Fermi energy. The higher the temperature, the higher the concentration of electrons. However, for a gas sensor, the sensing performance is not linearly dependent on the temperature. Due to the weak adsorption energy of target gas molecules and oxygen species (O_2^-, O^-, and O^{2-}) on the surface of the sensing material at a high temperature, chemisorbed target gas molecules and oxygen species would easily escape from the surface of the sensing materials at a higher temperature, which could reduce the sensing catalytic reaction. As a result, it is essential and crucial to investigate the best operating temperature of the as-prepared sensors based on FCN-MOSs.

Gas-sensing performances of sensors based on $Fe_7Co_{1.5}Ni_{1.5}$ and $Fe_6Co_2Ni_2$

Fig. 3a shows the curves of sensing properties *vs.* detection temperature, and the sensitivity has no discernible differences at low temperatures (from 50 to 150 °C). Then, the sensitivity increases significantly after 150 °C, with a maximum sensing value occurring at 250 °C. The sensitivities of $Fe_7Co_{1.5}Ni_{1.5}$ and
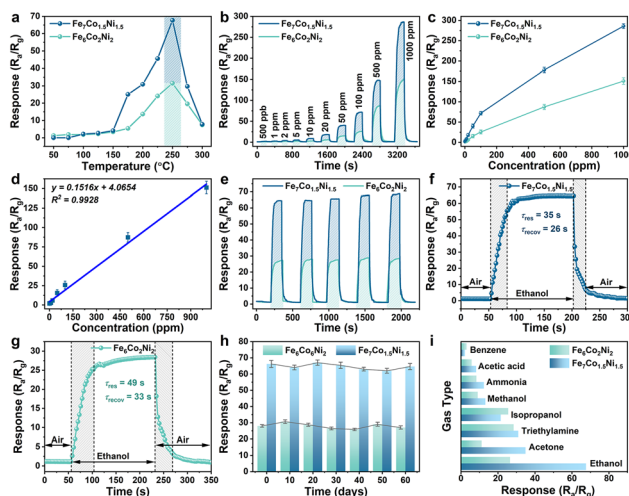
Fig. 3 Gas-sensing measurements: (a) response curves of $Fe_7Co_{1.5}Ni_{1.5}$ and $Fe_6Co_2Ni_2$ toward 100 ppm ethanol at different operating temperatures. (b) Dynamic response curves of $Fe_7Co_{1.5}Ni_{1.5}$ and $Fe_6Co_2Ni_2$ toward ethanol from 0.5 to 1000 pm at 250 °C. (c) Curves of response *vs.* concentration for $Fe_7Co_{1.5}Ni_{1.5}$ and $Fe_6Co_2Ni_2$. (d) Linear fitting of the response value as a function of ethanol concentration. (e) Reproducibility tests (five periods) of $Fe_7Co_{1.5}Ni_{1.5}$ and $Fe_6Co_2Ni_2$ toward 100 ppm ethanol at 250 °C. Response/recovery times of (f) $Fe_7Co_{1.5}Ni_{1.5}$ and (g) $Fe_6Co_2Ni_2$ towards 100 ppm ethanol at 250 °C, respectively. (h) Long-term repeatability tests of $Fe_7Co_{1.5}Ni_{1.5}$ and $Fe_6Co_2Ni_2$ toward 100 ppm ethanol. (i) Selectivity tests of $Fe_7Co_{1.5}Ni_{1.5}$ and $Fe_6Co_2Ni_2$ toward 100 ppm of different target gases at 250 °C.

$Fe_6Co_2Ni_2$ show rapid decreases from 250 to 300 °C. Therefore, the optimal operating temperature for the $Fe_7Co_{1.5}Ni_{1.5}$ and $Fe_6Co_2Ni_2$-based sensors are set at 250 °C.

Dynamic response–recovery curves of $Fe_7Co_{1.5}Ni_{1.5}$ and $Fe_6Co_2Ni_2$ in the ethanol concentration range from 0.5 to 1000 ppm are shown in Fig. 3b. Both gas sensors show good responses and recovery behaviors with various ethanol concentrations. With the increase of ethanol concentrations, the gas sensor responses exhibit a step-increasing pattern at the optimum working temperature of 250 °C. Compared to the $Fe_6Co_2Ni_2$ based sensor, the response of $Fe_7Co_{1.5}Ni_{1.5}$ is significantly increased with the concentration of targeted gases. These two sensors do not reach their saturation conditions when the ethanol concentration is 1000 ppm, as shown in Fig. 3c. In summary, the $Fe_7Co_{1.5}Ni_{1.5}$ based sensor has a better response than $Fe_6Co_2Ni_2$, owing to its optimal metal component ratio of Fe, Co, and Ni and the presence of the α-Fe_2O_3 phase. The LOD of the sensor to ethanol vapor was calculated utilizing a linear extrapolation of response sensitivity as a function of ethanol concentration (Fig. 3d). The calculated LOD result shows an ultra-low ethanol detection concentration of 30.7 ppb for $Fe_7Co_{1.5}Ni_{1.5}$ operated at 250 °C. The repeatability and stability of ethanol sensing were further investigated using $Fe_7Co_{1.5}Ni_{1.5}$ and $Fe_6Co_2Ni_2$. Fig. 3e shows that after five cycles of exposure to 100 ppm of ethanol at 250 °C, both $Fe_7Co_{1.5}Ni_{1.5}$ $Fe_6Co_2Ni_2$ show repeatable curves, indicating their good stability. Fig. 3f and g show the response and recovery times of $Fe_7Co_{1.5}Ni_{1.5}$ and $Fe_6Co_2Ni_2$ exposed to 100 ppm ethanol at 250 °C. The $Fe_7Co_{1.5}Ni_{1.5}$-based sensor has a response time (τ_{res}) of 35 s, which is faster than that (49 s) of $Fe_6Co_2Ni_2$. Both sensors need a short time to return to 90% of their original resistance (e.g., $Fe_7Co_{1.5}Ni_{1.5}$ needs 26 s and $Fe_6Co_2Ni_2$ needs 33 s). Because the thermal energy is generally smaller than the activation energy for desorption, most of the chemical sensors do not show good reversibility, resulting in a prolonged recovery time (τ_{recov}). The long-term stability of $Fe_7Co_{1.5}Ni_{1.5}$ and $Fe_6Co_2Ni_2$ was tested by exposing 100 ppm ethanol to the device once every ten days, measured at 250 °C for two months. Both the sensors show the preserved 98 percentage of their initial value with good stability after two months (Fig. 3h). Selectivity and cross-responses of these two sensors were investigated at 250 °C by exposing them to benzene (C_6H_6), acetic acid ($C_2H_4O_2$), ammonia (NH_3), methanol (CH_4O), isopropanol (C_3H_8O), trimethylamine (C_3H_9N), acetone (C_3H_6O), and ethanol (C_2H_6O) (all with a fixed volume of 100 ppm). The obtained results are shown in Fig. 3i.

The above results clearly indicate that these two sensors are more sensitive to ethanol than other gases, particularly the $Fe_7Co_{1.5}Ni_{1.5}$-based sensor. The phase of α-Fe_2O_3 can boost the redox process, whereas $Fe_7Co_{1.5}Ni_{1.5}$ can be applied as a catalyst according to previous reports.[24,33,34] Furthermore, the ethanol sensing properties of the sensor based on pristine α-Fe_2O_3 are shown in Fig. S10.† Fig. S10a† shows the response of α-Fe_2O_3 toward 100 ppm ethanol between 150 and 300 °C. The highest response (6.3) of ethanol gas was detected at 250 °C, indicating that the optimal operating temperature is

250 °C for α-Fe_2O_3, the same as the best working temperature of $Fe_7Co_{1.5}Ni_{1.5}$. Fig. S10b† shows the dynamic response curves of α-Fe_2O_3 at 250 °C for different ethanol vapor concentrations ranging from 5 to 1000 ppm. The result indicates that the response values of α-Fe_2O_3 increase dramatically with increasing ethanol concentration, especially when the concentration is above 500 ppm. Fig. S10c and d† show the calibration curve of α-Fe_2O_3 at various concentrations. The slope at 0–70 ppm is quite small, with a low response, increasing between 70 and 100 ppm. Generally, the pristine α-Fe_2O_3 based sensor shows poor gas-sensing performances for ethanol. Therefore, the combination of α-Fe_2O_3, $CoFe_2O_4$, and $NiFe_2O_4$ provides greater catalytic selectivity for the redox interactions between chemisorbed oxygen and ethanol molecules in the sensing material.

Gas-sensing performances of sensors based on $Fe_2Co_6Ni_2$ and $Fe_4Co_4Ni_2$

According to the aforementioned bipolar sensor design approach, the n-type sensing performance could be readily changed to p-type sensing performance by lowering the Fe element in the FCN-MOSs (e.g., $Fe_2Co_6Ni_2$ and $Fe_4Co_4Ni_2$).

The response-temperature curves of $Fe_2Co_6Ni_2$ and $Fe_4Co_4Ni_2$ toward 100 ppm ethanol operated at temperatures ranging from 50 to 300 °C are shown in Fig. 4a. Obviously, both $Fe_2Co_6Ni_2$ and $Fe_4Co_4Ni_2$ showed a p-type sensing behavior at their optimum working temperatures of 100 °C and
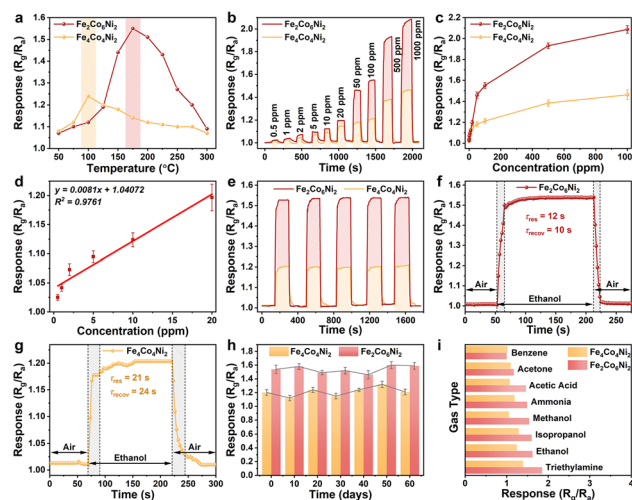
Fig. 4 Gas-sensing measurements: (a) response curves of $Fe_2Co_6Ni_2$ and $Fe_4Co_4Ni_2$ toward 100 ppm ethanol at different operating temperatures. (b) Dynamic response curves of $Fe_2Co_6Ni_2$ and $Fe_4Co_4Ni_2$ toward ethanol from 0.5 to 1000 pm at 250 °C. (c) Curves of response *vs.* concentration for $Fe_2Co_6Ni_2$ and $Fe_4Co_4Ni_2$. (d) Linear fitting of the response value as a function of ethanol concentration. (e) Reproducibility tests (five periods) of $Fe_2Co_6Ni_2$ and $Fe_4Co_4Ni_2$ toward 100 ppm ethanol at 250 °C. Response/recovery times of (f) $Fe_2Co_6Ni_2$ and (g) $Fe_4Co_4Ni_2$ towards 100 ppm ethanol at 250 °C, respectively. (h) Long-term repeatability tests of $Fe_2Co_6Ni_2$ and $Fe_4Co_4Ni_2$ toward 100 ppm ethanol. (i) Selectivity tests of $Fe_2Co_6Ni_2$ and $Fe_4Co_4Ni_2$ toward 100 ppm of different target gases at 250 °C.

175 °C. Still, their sensitivity was not as good as $Fe_7Co_{1.5}Ni_{1.5}$ and $Fe_6Co_2Ni_2$. The responses toward 100 ppm ethanol are 1.54 and 1.21 for these two sensors at their best operation temperatures of 100 °C and 175 °C, respectively. Because of a decrease in the Fe content, the amounts of p-type components in the $CoFe_2O_4$ and $NiFe_2O_4$ phases are increased. Therefore, sensors based on $Fe_2Co_6Ni_2$ and $Fe_4Co_4Ni_2$ exhibited a p-type sensing behavior.

Fig. 4b shows the dynamic response curves of $Fe_2Co_6Ni_2$ and $Fe_4Co_4Ni_2$ to ethanol with its concentration range of 0.5–1000 ppm. The response of $Fe_2Co_6Ni_2$ is about 1.1 to 1.4 times larger than that of $Fe_4Co_4Ni_2$. The response values as a function of ethanol concentration are shown in Fig. 4c, and they increase as the ethanol concentration increases. When the concentration is ~20 ppm, the $Fe_2Co_6Ni_2$ based sensor shows much larger response values. Because of the lower Fe ratio in the FCN-MOSs, $Fe_2Co_6Ni_2$ shows a more significant response than $Fe_4Co_4Ni_2$. A linear extrapolation was used to determine the LOD, and the results are shown in Fig. 4d. The obtained LOD for this sensor is 302.6 ppb. The repeatability of $Fe_2Co_6Ni_2$ and $Fe_4Co_4Ni_2$ samples' responses to 100 ppm ethanol was also studied for 5 successive cycles, and the results are shown in Fig. 4e. For these two sensors, the obtained curves are nearly identical, with average response values of 1.54 and 1.20, respectively. The responses can be entirely returned to their starting levels in each cycle.

Fig. 4f and g compare the response/recovery times (τ_{res}/τ_{recov}) of $Fe_2Co_6Ni_2$ and $Fe_4Co_4Ni_2$ toward 100 ppm ethanol at their optimum working temperatures (*i.e.*, 175 °C for $Fe_2Co_6Ni_2$ and 100 °C for $Fe_4Co_4Ni_2$). The $Fe_2Co_6Ni_2$-based sensor shows a faster response and recovery with its τ_{res}/τ_{recov} value of 12/10 s, much shorter than that of $Fe_4Co_4Ni_2$ (21/24 s). The $Fe_2Co_6Ni_2$ and $Fe_4Co_4Ni_2$-based sensors show much shorter τ_{res}/τ_{recov} values than those of the $Fe_7Co_{1.5}Ni_{1.5}$ and $Fe_6Co_2Ni_2$-based sensors, which can be attributed to their relatively lower response values.

The long-term repeatability testing results of $Fe_2Co_6Ni_2$ and $Fe_4Co_4Ni_2$ toward 100 ppm ethanol at the optimal testing temperature of 175 °C are shown in Fig. 4h. The sensitivity has not been changed significantly within 60 days, proving the long-term repeatability of $Fe_2Co_6Ni_2$ and $Fe_4Co_4Ni_2$.

Fig. 4i presents the selectivity testing results of $Fe_2Co_6Ni_2$ and $Fe_4Co_4Ni_2$ when exposed to 100 ppm of various types of gases at their optimal working temperatures. The $Fe_2Co_6Ni_2$-based sensor shows response values of 1.00, 1.17, 1.46, 1.49, 1.54, 1.60, 1.62, and 1.85 for benzene, acetone, acetic acid, ammonia, methanol, isopropanol, ethanol, and triethylamine gases, respectively. The results indicate that sensors based on $Fe_2Co_6Ni_2$ and $Fe_4Co_4Ni_2$ have a low selectivity towards ethanol gas.

Discussions on the gas-sensing mechanism

Table 1 compares ethanol sensing performances of various MOF-derived MOS-based sensors reported in the literature, including MOF-derived porous TiO_2, MOF-derived CuO, MOF-derived Ga-doped Co_3O_4, zirconium-based MOFs, ZIF-67-derived $Co_3O_4/NiCo_2O_4$, and ZIF-8 MOF-derived ZnO. Based on Table 1, our newly developed FCN-MOS-based sensor can be operated at a relatively low working temperature and achieve a faster dynamic response with a higher sensitivity to ethanol. The main reasons are attributed to the novel MOF-derived nanostructures and the optimum proportion of the catalysts of α-Fe_2O_3, $CoFe_2O_4$, and $NiFe_2O_4$ phases, which can provide an effective gas diffusion path *via* a well-aligned porous structure.

Fig. 5 schematically illustrates the adsorption of gas molecules, transfer of electrons, and surface reaction processes of FCN-MOS-derived oxide materials in air and ethanol gases, respectively. Generally, for the n-type sensing mechanism, when a sensing material is exposed to air, oxygen molecules are adsorbed and ionized. Thus, oxygen species such as O_2^-, O^-, and O^{2-} exist on the surface. During the oxygen ionization process, the electron concentration in a conductive band (E_c) reduces, then the resistance of the sensing material increases significantly. Therefore, the R_a value is increased. For a p-type sensor, electron extraction would produce a hole accumulation layer near the surface. Accordingly, the R_a value is decreased. Within the detection environment, with the gas such as ethanol in this study, depending on n- or p-types, the thickness of the electron (or hole) accumulation layer decreases (or
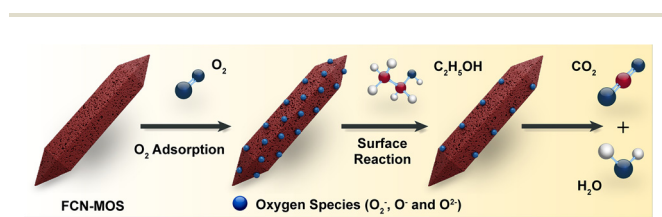

Fig. 5 Schematic diagram of the ethanol gas-sensing mechanism of an FCN-MOS.

Table 1 Comparison between the ethanol sensing performance of MOF-derived MOSs

Materials	Temperature (°C)	Concentration (ppm)	Response (S)	τ_{res}/τ_{recov} (s/s)
MOF-derived porous TiO_2[35]	250	500	~46	74/102
MOF-derived CuO[36]	275	100	12.1	102/40
MOF-derived Ga-doped Co_3O_4[37]	180	50	~118	3/15
Zirconium-based MOF[38]	150	100	~1.4	~50/400
ZIF-67-derived $Co_3O_4/NiCo_2O_4$[39]	180	100	26	~4/~6
ZIF-8-derived ZnO[40]	300	1	6.7	1/28.5
FCN-MOSs (this work)	250	100	71.9	35/26

increases) based on the reaction of CH_3CH_2OH (gas) + $8O^-$ (ads) → $3CO_2$ + $3H_2O$ + $8e^-$. The ethanol molecules transfer electrons to the n-type (α-Fe_2O_3) or p-type material (such as $CoFe_2O_4$ and $NiFe_2O_4$ phases), leading to a decrease/increase in electrical resistance, respectively.

According to the literature, p–n sensing mode transition is mainly related to the work function variations caused by the targeted gases.[41] Kim et al. studied the p–n transition for CuO nanowires as a function of operating temperature for detecting the NO_2 gas.[42] In this study, the gas sensing transition from n-type to p-type is mainly due to the changes in the polarity of the sensing material, which means that the polarity of the sensing material can be changed from n-type to p-type when the phase composition of α-Fe_2O_3 (n-type) or $CoFe_2O_4$, and $NiFe_2O_4$ material (p-type) phases can be finely changed.

Conclusions

In summary, a series of Fe-MIL-88B-derived trimetallic FeCoNi oxides (FCN-MOS) were successfully synthesized using a one-step hydrothermal reaction with subsequent calcination treatment. The FCN-MOS system consists of α-Fe_2O_3, $CoFe_2O_4$, and $NiFe_2O_4$ and exhibits an elongated hexagonal rod-like structure with abundant mesopores. In addition, by altering the Fe, Co, and Ni ratio, the nanostructure and pore size of FCN-MOS can be effectively tuned, and a transition of gas-sensing behavior from n- to p-type can be achieved. The sensor based on FCN-MOS (Fe : Co : Ni = 7 : 1.5 : 1.5) exhibits excellent gas-sensing performance for ethanol, including high response (S = 71.9), long-term stability (over 60 days), and good selectivity, as well as a low detection limit of 500 ppb. The unique mesoporous structure and synergic effects of the α-Fe_2O_3, $CoFe_2O_4$, and $NiFe_2O_4$ phases are primarily responsible for the enhanced sensing performance. Overall, this work provides a facile route for synthesizing MOF-derived metal oxide semiconductors and proposes a novel material design strategy.

Conflicts of interest

There are no conflicts to declare.

Acknowledgements

References

1 D. P. Erdosy, M. B. Wenny, J. Cho, C. DelRe, M. V. Walter, F. Jiménez-Ángeles, B. Qiao, R. Sanchez, Y. Peng, B. D. Polizzotti, M. O. de la Cruz and J. A. Mason, Nature, 2022, 608, 712–718.

2 S. Zhou, O. Shekhah, A. Ramírez, P. Lyu, E. Abou-Hamad, J. Jia, J. Li, P. M. Bhatt, Z. Huang, H. Jiang, T. Jin, G. Maurin, J. Gascon and M. Eddaoudi, Nature, 2022, 606, 706–712.

3 S. Wang, W. Xie, P. Wu, G. Lin, Y. Cui, J. Tao, G. Zeng, Y. Deng and H. Qiu, Nat. Commun., 2022, 13, 6673.

4 H. K. Lee, C. S. Koh, W.-S. Lo, Y. Liu, I. Y. Phang, H. Y. Sim, Y. H. Lee, G. C. Phan-Quang, X. Han, C.-K. Tsung and X. Y. Ling, J. Am. Chem. Soc., 2020, 142, 11521–11527.

5 T. Devic and C. Serre, Chem. Soc. Rev., 2014, 43, 6097–6115.

6 C. Serre, C. Mellot-Draznieks, S. Surblé, N. Audebrand, Y. Filinchuk and G. Férey, Science, 2007, 315, 1828–1831.

7 P. Horcajada, F. Salles, S. Wuttke, T. Devic, D. Heurtaux, G. Maurin, A. Vimont, M. Daturi, O. David, E. Magnier, N. Stock, Y. Filinchuk, D. Popov, C. Riekel, G. Férey and C. Serre, J. Am. Chem. Soc., 2011, 133, 17839–17847.

8 W. Li, X. Guo, P. Geng, M. Du, Q. Jing, X. Chen, G. Zhang, H. Li, Q. Xu, P. Braunstein and H. Pang, Adv. Mater., 2021, 2105163.

9 M. Kim, R. Xin, J. Earnshaw, J. Tang, J. P. Hill, A. Ashok, A. K. Nanjundan, J. Kim, C. Young, Y. Sugahara, J. Na and Y. Yamauchi, Nat. Protoc., 2022, 17, 2990–3027.

10 V. Pascanu, G. González Miera, A. K. Inge and B. Martín-Matute, J. Am. Chem. Soc., 2019, 141, 7223–7234.

11 X. Wang, H. Xiao, A. Li, Z. Li, S. Liu, Q. Zhang, Y. Gong, L. Zheng, Y. Zhu, C. Chen, D. Wang, Q. Peng, L. Gu, X. Han, J. Li and Y. Li, J. Am. Chem. Soc., 2018, 140, 15336–15341.

12 Q. Qian, Y. Li, Y. Liu, L. Yu and G. Zhang, Adv. Mater., 2019, 31, 1901139.

13 X. Xu, J. Liu, J. Liu, L. Ouyang, R. Hu, H. Wang, L. Yang and M. Zhu, Adv. Funct. Mater., 2018, 28, 1707573.

14 W. Xie, Y. Ren, B. Yu, X. Yang, M. Gao, J. Ma, Y. Zou, P. Xu, X. Li and Y. Deng, Small, 2021, 17, 2103176.

15 L. Lüder, A. Gubicza, M. Stiefel, J. Overbeck, D. Beretta, A. Sadeghpour, A. Neels, P. N. Nirmalraj, R. M. Rossi, C. Toncelli and M. Calame, Adv. Electron. Mater., 2022, 8, 2100871.

16 H. T. Jung, ACS Sens., 2022, 7, 912–913.

17 S. Y. Jeong, J. S. Kim and J. H. Lee, Adv. Mater., 2020, 32, e2002075.

18 A. Bag, M. Kumar, D.-B. Moon, A. Hanif, M. J. Sultan, D. H. Yoon and N.-E. Lee, Sens. Actuators, B, 2021, 346, 130463.

19 S. Cao, Y. Xu, Z. Yu, P. Zhang, X. Xu, N. Sui, T. Zhou and T. Zhang, Small, 2022, 2203715.

20 L. Wang, Y. Wang, H. Tian, L. Qiao and Y. Zeng, Sens. Actuators, B, 2020, 314, 128085.

21 W. Remlalfaka, C. Murugesan, P. N. Anantharamaiah and N. Manikanda Prabu, Ceram. Int., 2021, 47, 11526–11535.

22 N. Zhang, S. Ruan, F. Qu, Y. Yin, X. Li, S. Wen, S. Adimi and J. Yin, *Sens. Actuators, B*, 2019, **298**, 126887.

23 S. Zhang, W. Jiang, Y. Li, X. Yang, P. Sun, F. Liu, X. Yan, Y. Gao, X. Liang, J. Ma and G. Lu, *Sens. Actuators, B*, 2019, **291**, 266–274.

24 T. Zhou, R. Zhang, Y. Wang and T. Zhang, *Sens. Actuators, B*, 2019, **281**, 885–892.

25 G. Lee, S. Lee, S. Oh, D. Kim and M. Oh, *J. Am. Chem. Soc.*, 2020, **142**, 3042–3049.

26 D. Bara, E. G. Meekel, I. Pakamore, C. Wilson, S. Ling and R. S. Forgan, *Mater. Horiz.*, 2021, **8**, 3377–3386.

27 X. Zhang, G. Li, Y. Zhang, D. Luo, A. Yu, X. Wang and Z. Chen, *Nano Energy*, 2021, **86**, 106094.

28 Z. Dai, C.-S. Lee, Y. Tian, I.-D. Kim and J.-H. Lee, *J. Mater. Chem. A*, 2015, **3**, 3372–3381.

29 J. Chen, J. Zheng, Q. Huang, F. Wang and G. Ji, *ACS Appl. Mater. Interfaces*, 2021, **13**, 36182–36189.

30 H. B. Zheng, H. H. Chen, Y. L. Wang, P. Z. Gao, X. P. Liu and E. V. Rebrov, *ACS Appl. Mater. Interfaces*, 2020, **12**, 45987–45996.

31 X.-Y. Huang, Z.-T. Chi, W. Yang, Y. Deng and W.-F. Xie, *Sens. Actuators, B*, 2022, **361**, 131715.

32 S. Sze and K. K. Ng, in *Physics of Semiconductor Devices*, 2006, pp. 5–75, DOI: **10.1002/9780470068328.ch1**.

33 P. Wang, S. Z. Wang, Q. Han, D. Q. Zou, W. K. Zhao, X. D. Wang, C. Luo, X. Yang, X. Wu and W. F. Xie, *Adv. Mater. Interfaces*, 2020, **8**, 2001831.

34 D. Xie, F. Zhang, G. Dai, Z. Mao, K. Yu and F. Qu, *New J. Chem.*, 2022, **46**, 11368–11376.

35 Y. Zhang, J. Zhang, G. Li, D. Leng, W. Wang, Y. Gao, J. Gao, Q. Liang, H. Lu and C. Wang, *J. Mater. Sci.: Mater. Electron.*, 2019, **30**, 17899–17906.

36 S. Wang, Z. Gao, G. Song, Y. Yu, W. He, L. Li, T. Wang, F. Fan, Y. Li, L. Zhang, X. Zhang, Y. Fu and W. Qi, *J. Mater. Chem. C*, 2020, **8**, 9671–9677.

37 H. Sun, X. Tang, J. Zhang, S. Lia and L. Liu, *Sens. Actuators, B*, 2021, **346**, 130546.

38 J. H. Lee, T. T. T. Nguyen, L. H. T. Nguyen, T. B. Phan, S. S. Kim and T. L. H. Doan, *J. Hazard. Mater.*, 2021, **403**, 124104.

39 Y. Tao and W. Zeng, *Ceram. Int.*, 2021, **47**, 8441–8446.

40 Y. Xia, A. Pan, D. W. Gardner, S. Zhao, A. K. Davey, Z. Li, L. Zhao, C. Carraro and R. Maboudian, *Sens. Actuators, B*, 2021, **344**, 130180.

41 A. Gurlo, N. Bârsan, A. Oprea, M. Sahm, T. Sahm and U. Weimar, *Appl. Phys. Lett.*, 2004, **85**, 2280–2282.

42 Y.-S. Kim, I.-S. Hwang, S.-J. Kim, C.-Y. Lee and J.-H. Lee, *Sens. Actuators, B*, 2008, **135**, 298–303.